



Published in final edited form as:

Cell Rep. 2018 March 13; 22(11): 2898–2908. doi:10.1016/j.celrep.2018.02.064.

## Functional Compartmentalization within Starburst Amacrine Cell Dendrites in the Retina

Alon Poleg-Polsky<sup>1,2,4</sup>, Huayu Ding<sup>1,3,4</sup>, and Jeffrey S. Diamond<sup>1,5,\*</sup>

<sup>1</sup>Synaptic Physiology Section, National Institute of Neurological Disorders and Stroke, NIH, 35 Convent Drive, Building 35A, Room 3E-621, Bethesda, MD 20892, USA

### SUMMARY

Dendrites in many neurons actively compute information. In retinal starburst amacrine cells, transformations from synaptic input to output occur within individual dendrites and mediate direction selectivity, but directional signal fidelity at individual synaptic outputs and correlated activity among neighboring outputs on starburst dendrites have not been examined systematically. Here, we record visually evoked calcium signals simultaneously at many individual synaptic outputs within single starburst amacrine cells in mouse retina. We measure visual receptive fields of individual output synapses and show that small groups of outputs are functionally compartmentalized within starburst dendrites, creating distinct computational units. Inhibition enhances compartmentalization and directional tuning of individual outputs but also decreases the signal-to-noise ratio. Simulations suggest, however, that the noise underlying output signal variability is well tolerated by postsynaptic direction-selective ganglion cells, which integrate convergent inputs to acquire reliable directional information.

### In Brief

This is an open access article under the CC BY-NC-ND license (<http://creativecommons.org/licenses/by-nc-nd/4.0/>).

\*Correspondence: [diamondj@ninds.nih.gov](mailto:diamondj@ninds.nih.gov).

<sup>2</sup>Present address: Department of Physiology and Biophysics, University of Colorado School of Medicine, Aurora, CO 80045, USA

<sup>3</sup>Present address: Apple, Inc., Cupertino, CA 95014, USA

<sup>4</sup>These authors contributed equally

<sup>5</sup>Lead Contact

### SUPPLEMENTAL INFORMATION

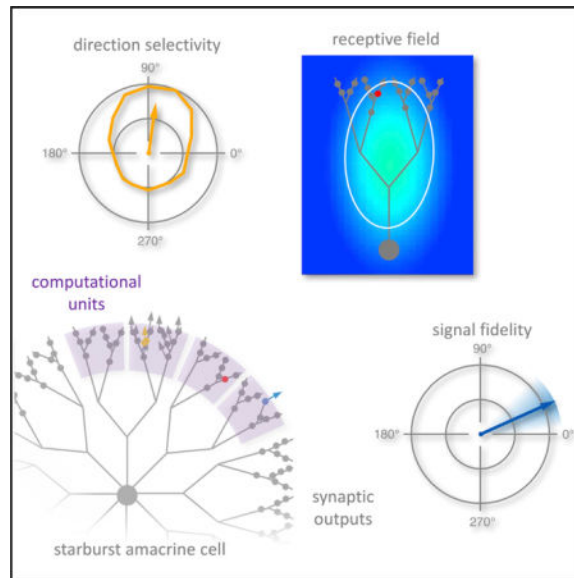
Supplemental Information includes five figures and can be found with this article online at <https://doi.org/10.1016/j.celrep.2018.02.064>.

### AUTHOR CONTRIBUTIONS

Conceptualization, H.D., A.P.-P., and J.S.D.; Methodology, H.D., A.P.-P., and J.S.D.; Software, H.D. and A.P.-P.; Formal Analysis, A.P.-P. and J.S.D.; Investigation, H.D. and A.P.-P.; Writing – Original Draft, H.D. and J.S.D.; Writing – Review & Editing, A.P.-P. and J.S.D.; Visualization, H.D., A.P.-P. and J.S.D.; Supervision, J.S.D.; Funding Acquisition, J.S.D.

### DECLARATION OF INTERESTS

The authors declare no competing interests.



Poleg-Polsky et al. examine the directional signaling fidelity of individual synapses on starburst amacrine cell dendrites. They identify functionally and morphologically distinct signaling compartments within SAC dendrites and show that inhibition enhances reliable decoding by postsynaptic directionselective ganglion cells.

## INTRODUCTION

Neurons typically receive synaptic inputs onto their dendritic branches and funnel postsynaptic signals to the soma, where they are transformed into an output pattern of action potentials in the axon. In many cases, morphology; active conductances; and diverse, specifically positioned and timed synaptic inputs confer some computational autonomy to individual dendrites within a single cell (Branco et al., 2010; Euler et al., 2002; Häusser and Mel, 2003; London and Häusser, 2005; Stuart and Spruston, 2015), although the outputs of dendritic compartments ultimately are pooled together into a common spike pattern. By contrast, in amacrine cells—typically axonless, non-spiking interneurons in the retina—synaptic inputs and outputs arrive on and depart from the same dendritic branches, enabling visual information to be processed via many parallel channels within the same cell, often without involving the soma (Grimes et al., 2010; Hausselt et al., 2007).

Despite a growing appreciation for the complexity of dendritic signaling, it remains difficult in most neurons to link particular dendritic calculations to specific, physiologically relevant computational tasks. One notable exception is the starburst amacrine cell (SAC), a radially symmetric interneuron that provides directionally tuned GABAergic inhibition to direction-selective ganglion cells (DSGCs; Famiglietti, 1991). SAC dendrites respond preferentially to “outward” (or “centrifugal”) visual motion, i.e., light stimuli moving in the direction from the soma to the dendritic tips (Euler et al., 2002; Hausselt et al., 2007; Lee and Zhou, 2006), so that different dendritic regions within the same cell prefer different directions (Euler et al., 2002; Hausselt et al., 2007; Vlasits et al., 2016). Each DSGC receives inhibitory synapses from many SAC dendrites tuned roughly to the same direction (Briggman et al.,

2011), thereby causing the DSGC to prefer the opposite direction (Briggman et al., 2011; Fried et al., 2002; Lee et al., 2010; Poleg-Polsky and Diamond, 2016b; Vaney et al., 2012).

SACs receive excitatory and inhibitory synaptic inputs on their proximal dendrites and make GABAergic outputs from distinct varicosities on distal dendrites (Ding et al., 2016; Famiglietti, 1991). Multiple mechanisms may contribute to dendritic direction selectivity (DS) in SACs, including intrinsic morphological and biophysical characteristics (Gavrikov et al., 2003; Hausselt et al., 2007; Oesch and Taylor, 2010; Tukker et al., 2004), non-uniform excitatory input from different bipolar cell types (Fransen and Borghuis, 2017; Kim et al., 2014), and lateral inhibition from neighboring amacrine cells (Lee and Zhou, 2006; Münch and Werblin, 2006), but the relative importance of these different mechanisms remains unclear. In addition, the SAC's fundamental computational unit—a region of the dendritic arbor within which synapses convey the same visual information—has not been determined. SACs may possess just a few functional units, each perhaps corresponding to one of the four cardinal directions encoded by DSGCs (Koren et al., 2017), or maybe comprising all branches arising from a single primary dendrite (Masland, 2005); at the other extreme, individual output varicosities might operate independently, as in A17 amacrine cells (Grimes et al., 2010).

Here, we apply  $\text{Ca}^{2+}$  imaging to examine directional signaling simultaneously in many individual output varicosities within a region of a SAC dendritic arbor. We find that, although varicosities sharing a common primary dendrite exhibit largely overlapping receptive fields, response correlations reveal distinct computational units comprising small groups of varicosities. Blocking GABAergic inhibition reduces functional compartmentalization and directional tuning but also improves the signal-to-noise ratio (SNR). Numerical simulations suggest that response variability in individual SAC varicosities arises from stochastic synaptic and/or channel properties rather than labile directional tuning (Rivlin-Etzion et al., 2012) and that this variability does not compromise signal fidelity in DSGCs, which integrate inhibitory inputs from many SACs. These results highlight the SAC's distributed, parallel input-output (I/O) properties and show how inhibition enhances a key visual computation in the retina.

## RESULTS

### Receptive Field Characteristics of Individual Varicosities

SACs were imaged in whole-mount retinas from mice expressing tdTomato under the control of the choline acetyltransferase (ChAT) reporter, which labels SACs specifically in the retina (Figure 1; Ivanova et al., 2010). To visualize single ON SAC dendritic arbors, individual tdTomato-positive somata in the ganglion cell layer were iontophoretically injected with Oregon Green BAPTA-1 (OGB1) via a sharp electrode (Figure 1A; Experimental Procedures). Although OGB1 fluorescence is  $\text{Ca}^{2+}$  dependent, baseline signal was usually sufficient to visualize the dendritic arbor (Figure 1A), which exhibited highly consistent geometry across SACs (Figure S1).

Typically, a visual receptive field (RF) is a property of an entire neuron and is defined as the region in visual space over which a visual stimulus evokes a response, usually recorded in

the soma or axon (Hartline, 1938). Recently, subcellular RF measurements have been made in retinal bipolar cell terminals (Behrens et al., 2016). Here, we measured RF properties of individual output varicosities to examine the distributed I/O characteristics of SAC dendrites. First, we confirmed that light-evoked  $\text{Ca}^{2+}$  responses in individual varicosities could be evaluated independently. We imaged a region of an OGB1-filled SAC dendritic arbor and measured fluorescent  $\text{Ca}^{2+}$  transients evoked by stationary or moving bars of light (e.g., Figures 1B–1D). During the first 1 s following response onset,  $\text{Ca}^{2+}$  signals were highest in the varicosity and decreased along the dendrite with a length constant ( $\lambda$ ) of  $0.68 \pm 0.18 \mu\text{m}$  ( $n = 10$  varicosities from 2 SACs), much less than the average distance between neighboring varicosities ( $3.1 \pm 1.2 \mu\text{m}$ , mean  $\pm$  SEM;  $n = 72$  varicosities from 6 SACs; Figures 1B–1D).  $\text{Ca}^{2+}$  signals were, therefore, sufficiently localized to permit responses in individual varicosities to be evaluated independently.

In mouse retina, SACs receive excitatory and inhibitory inputs on proximal dendrites and make synaptic outputs at varicosities on distal dendrites (Ding et al., 2016; Vlasits et al., 2016), suggesting that each varicosity's RF may be spatially offset relative to its physical location. To test this, we measured fluorescent  $\text{Ca}^{2+}$  transients evoked by stationary bars of light presented at various positions and angles. The spatial RF of each varicosity was reconstructed (Johnston et al., 2014; Experimental Procedures) to yield a contour plot of the RF (Figures 1E and 1F). Two-dimensional Gaussian fits determined the RF center location; size (full width at half maximum [FWHM]:  $110 \pm 16 \mu\text{m}$ ; Experimental Procedures; Figures 1F and 1I); and shape, which was typically elliptical, with the major axis roughly aligned along the line through the varicosity and the soma (Figure 1E). RF centers invariably were located between the varicosity and the soma ( $25 \pm 13 \mu\text{m}$  from the soma;  $n = 69$  varicosities from 4 cells; Figures 1E, 1G, and 1H), consistent with more proximal locations of excitatory inputs (Ding et al., 2016; Famiglietti, 1991; Vlasits et al., 2016).

Surround inhibition shapes the RF properties of many cells in the retina (Kuffler, 1953; Werblin and Dowling, 1969). Inhibition could shape the RFs of SAC varicosities via lateral connectivity with other amacrine cells (Ding et al., 2016; Kostadinov and Sanes, 2015; Lee and Zhou, 2006) or via inhibitory feedback synapses from amacrine cells onto presynaptic bipolar cell terminals (Eggers and Lukasiewicz, 2011). Inhibitory synaptic inputs onto SACs are mediated by  $\text{GABA}_A$  receptors (Chen et al., 2016; Kostadinov and Sanes, 2015; Lee and Zhou, 2006), so we tested the effects of a selective  $\text{GABA}_A$  receptor antagonist (SR95531,  $25 \mu\text{M}$ ) on the RF dimensions of SAC varicosities. Bath application of SR95531 increased the amplitude of light-evoked  $\text{Ca}^{2+}$  transients at the RF center (to  $227 \pm 79\%$  of control;  $n = 69$ ;  $p < 1 \times 10^{-16}$ ; e.g., Figure 1F) and expanded the RF Gaussian contour (FWHM:  $133 \pm 26\%$  of control;  $n = 69$ ;  $p = 1.1 \times 10^{-16}$ ; Figure 1I) without significantly changing the average location of RF centers relative to the soma ( $p = 0.4$ ;  $n = 69$ ; e.g., Figures 1G and 1H). We did not detect significant effects of SR95531 on light-evoked  $\text{Ca}^{2+}$  responses in type 5 cone bipolar cell (CBC5) terminals, which provide a portion of the excitatory input to ON SACs (Ding et al., 2016; Kim et al., 2014; Figure S2). Although we could not verify that the recorded CBC5s were connected to SACs, and we did not record from all ON CBC5 types that contact ON SACs (Ding et al., 2016; Kim et al., 2014), our results with CBC5 suggest that SR95531's effects on SAC  $\text{Ca}^{2+}$  responses reflect, primarily, blockade of lateral inhibition from other amacrine cells.

## Response Correlations Reveal Distinct Computational Units within SAC Dendrites

Our RF analysis indicated that varicosities within a large dendritic region exhibit overlapping RFs. This could mean that all of the varicosities in a region — perhaps those on branches arising from a common primary dendrite—constitute a single computational unit and transmit essentially identical visual information (Masland, 2005). If this were true, varicosities sharing a common primary dendrite should exhibit correlated visual responses.

To test this, we filled individual SACs with OGB1 and recorded  $\text{Ca}^{2+}$  signals simultaneously from numerous varicosities in the same dendritic region in response to light bars moving in each of eight different directions (Figure 2). Each stimulus direction was repeated in multiple trials. The average  $\text{Ca}^{2+}$  signal during the first 1 s of each response was measured individually in each varicosity, and the correlation coefficient of response amplitudes between every varicosity pair was calculated (Figure 2B; Experimental Procedures). Noise analyses confirmed that most trial-to-trial response variability was due to biological noise (Figure S3).

Based on response correlations, varicosities were hierarchically clustered into distinct functional groups (Experimental Procedures). In the illustrated cell, four clusters were identified within the imaged region (colored boxes, Figure 2B). Although clustering was blind to morphology, varicosities within functionally identified clusters were consistently co-localized within dendrites arising from common branch points and were morphologically separated from varicosities in other clusters (varicosity colors in Figure 2A correspond to boxed clusters in Figure 2B*i*). Similar results were obtained in 16 cells. In many cases, multiple clusters shared common primary or secondary parent branches (e.g., the yellow and green clusters in Figure 2A), suggesting that the number of distinct functional groups—putative “computational units”—within an SAC substantially exceeds the number of primary dendritic branches. Accordingly, the geometric locations of varicosities, measured by the angle of the segment connecting each to the soma, spanned a relatively small range within clusters ( $\sigma_{\text{angle}} = 8.6 \pm 4.5^\circ$ ,  $n = 26$  clusters); given some angular overlap between neighboring clusters (Figure 2A), these results suggest that each  $360^\circ$  SAC dendritic arbor contains ~20 functional compartments. As ON SACs make 250-300 synaptic outputs (Ding et al., 2016), each compartment may contain, on average, 10-15 synaptic varicosities. This value agrees roughly with the number of varicosities in functionally identified clusters ( $8.7 \pm 4.5$  varicosities;  $n = 26$  clusters), considering that we likely failed to image every varicosity within each cluster.

Because visual responses were evoked with moving bars, functional clusters could reflect similar direction preference among neighboring varicosities. To test this, we computed the mean response in each varicosity to multiple presentations of the same stimulus direction and then subtracted the mean from each response to isolate trial-to-trial variability, thereby eliminating directional bias (Figure 2B*ii*). Residual correlations yielded similar clusters to those derived from raw responses (cf. Figures 2B*i* and 2B*ii*), suggesting that functional compartments arise primarily due to electrotonic proximity or common synaptic input rather than similar DS.

Next, we evaluated how correlations within and between varicosities vary with the number of branch points separating them (Figure 2D). Within a single branch, varicosities were divided into distal and proximal groups, and correlations were evaluated within and between these groups. In other cases, correlations were evaluated between all varicosities within  $x$  branch points of each other ( $C_{\text{within}}$ ) and between varicosities separated by exactly  $x$  branch points ( $C_{\text{between}}$ ; schematics shown for a single varicosity; Figure 2D). Functional unity was indicated by a  $C_{\text{within}}:C_{\text{between}}$  ratio (the McClain-Rao index; McClain and Rao, 1975) near 1, which was observed between varicosities separated by fewer than two branch points (Figure 2C). Accordingly, correlation between varicosities decreased with intervening dendritic distance ( $\lambda=110\mu\text{m}$ ; Figure 2E).

SR95531 application did not eliminate functionally distinct clusters (Figures 2B*iii* and 2B*iv*), but it did decrease correlations within clusters and increase correlations between clusters (Figures 2B–2E), suggesting that inhibition enhances functional compartmentalization of SAC dendrites.

### DS Tuning among Varicosities within the Same Compartment

DSGCs compute direction by selectively contacting SAC dendrites tuned to the DSGC's null direction (ND; Briggman et al., 2011). The fidelity of the computation depends on many factors, including the strength and variability of DS signals in SAC varicosities. Previous studies showed that individual varicosities are directionally tuned (Euler et al., 2002; Vlasits et al., 2016). Here, we measured the strength and variability of DS between individual SAC varicosities within the same dendritic region and examined how these parameters are influenced by synaptic inhibition (Figure 3).  $\text{Ca}^{2+}$  signals in OGB1-filled SACs were recorded in individual varicosities in response to moving bars (Figures 3A and 3B), and the preferred direction (PD) was determined from the vector sum of averaged responses to motion in 8 different directions (Taylor and Vaney, 2002; Figure 3B). As reported previously (Euler et al., 2002; Vlasits et al., 2016), individual varicosities responded selectively to centrifugal (outward) motion relative to the SAC soma (Figures 3B and 3C), although varicosities within an imaged dendritic region exhibited variable PDs (SD of individual varicosity PD relative to the average PD in varicosities across the imaged dendritic region,  $\sigma_{\text{PD}} = 44.8^\circ$ ;  $n = 394$  varicosities in 12 SACs; e.g., Figure 3C). Within functional compartments, defined as described earlier (Figure 2), measured PD values of individual varicosities were more consistent (inter-varicosity  $\sigma_{\text{PD}} = 28 \pm 22^\circ$ ;  $n = 26$  compartments; Figure 3D), exhibiting variability within our PD measurement error (Figure S3E). To a first approximation, then, varicosities within a functional compartment exhibited very similar (possibly identical) directional tuning.

DS depends upon the relative size of PD and ND responses and the sharpness of directional tuning, attributes that are often combined into a direction selectivity index (DSI) calculated from the summed response vector. Here, we considered the strength and sharpness of DS separately: DSI was calculated as a ratio of responses to PD and ND stimuli (Experimental Procedures) and was calculated for each varicosity individually (Figure 3F); tuning width, determined from a Gaussian fit to response amplitude versus stimulus direction, was calculated as the FWHM of the average fit to responses in all varicosities imaged in each



SAC (Experimental Procedures; Figures 3G and 3H). The DSI of individual varicosities ( $0.66 \pm 0.17$ ;  $n = 394$  varicosities from 12 SACs; Figure 3F) was higher than that of inhibitory postsynaptic currents (IPSCs) in DSGCs (0.37; Fried et al., 2002; Poleg-Polsky and Diamond, 2016a), suggesting that DS tuning of IPSCs in DSGCs is limited more by the broad tuning curve of varicosities ( $133 \pm 26^\circ$ ;  $n = 12$  cells; Figures 3G and 3H) and the variability between individual SAC outputs than their DS tuning strength.

SR95531 increased inter-varicosity  $\sigma_{PD}$  within compartments ( $p = 0.03$ , paired t test; Figure 3E), reduced varicosity DSI (to  $0.44 \pm 0.17$ ;  $n = 394$ ;  $p < 1 \times 10^{-16}$  versus control; Figure 3F), and broadened the DS tuning curve (to  $217 \pm 82^\circ$ ;  $n = 12$  cells;  $p = 0.0015$  versus control; Figures 3G and 3H). These findings confirm, at the level of single synaptic varicosities, previous reports that blocking inhibition reduces DS in SAC dendrites (Chen et al., 2016; Ding et al., 2016; Lee and Zhou, 2006).

### Signaling Noise Degrades DS Fidelity in SAC Varicosities

As noted earlier, individual varicosities responded variably to repeated presentations of the same stimulus (Figure S3). Under control conditions, the SNR ( $\sqrt{\text{mean}^2/\sigma^2}$ ) of the PD response was just  $2.0 \pm 0.5$  ( $n = 16$  SACs; Figure 4A). SR95531 application increased the SNR to  $4.0 \pm 1.0$  ( $p = 2.7 \times 10^{-7}$ , paired t test;  $n = 16$ ; Figure 4A), primarily reflecting an increase in response amplitude ( $195 \pm 66\%$  of control;  $p = 2.4 \times 10^{-6}$ , paired t test;  $n = 16$ ; Figure 4B), with little change in biological variability ( $134 \pm 55\%$  of control;  $p = 0.11$ , paired t test;  $n = 16$ ; Figure 4C). To quantify the impact of response variability on DS signaling fidelity, we examined tuning curves constructed from eight consecutive single responses to eight different directions of motion in a single varicosity (Figure 4D), and we determined the PD for each round of responses from the summed response vector (Figure 4E). A perfect direction sensor would report the same PD for each round, whereas a less reliable detector would report variable PDs. We measured DS response fidelity by calculating the SD of single-round PD values (intra-varicosity  $\sigma_{PD}$ ) in each varicosity and then averaged the  $\sigma_{PD}$  values across all varicosities recorded in each of 16 cells. This analysis indicated substantial intra-varicosity variability in calculated PD ( $\sigma_{PD} = 48 \pm 8^\circ$ ;  $n = 16$ ) that was not significantly different in the presence of SR95531 ( $\sigma_{PD} = 49 \pm 12^\circ$ ;  $n = 16$ ;  $p = 0.69$  versus control, paired t test; Figure 4F). These results indicate that blocking inhibition exerted opposing effects on DS signaling in SAC varicosities: SR95531 reduced DSI (Figure 3F) but enhanced SNR (Figure 4A), leading to negligible changes in DS fidelity within individual varicosities, at least as measured by  $\sigma_{PD}$ . These results also suggest that the SR95531-induced increase in PD variability between varicosities within functional compartments (Figure 3E) was not due to PD measurement error.

### Downstream Effects on DS Fidelity Depend on the Noise Source

To examine the impact of SAC signaling noise on downstream computations, we next constructed a mathematical model incorporating realistic SAC-DSGC connectivity (Briggman et al., 2011; Figure S4) and the SAC varicosity response characteristics observed here (Figure 5). The model comprised 100 SACs arrayed above one DSGC dendritic arbor; inhibitory inputs to the DSGC were chosen stochastically from among SAC varicosities that

overlapped the DSGC arbor and were aligned with the DSGC's ND (Briggman et al., 2011; Experimental Procedures). In 1,000 simulations,  $23 \pm 2$  presynaptic SACs provided a total of  $123 \pm 5$  synapses onto the DSGC. Responses in each SAC varicosity depended on the direction of the motion stimulus relative to that varicosity's DS tuning curve. SAC inputs were summed linearly to produce a DSGC IPSC that, in the absence of SAC variability, exhibited a DSI (0.53; Figure 5C) that was less than that of the individual varicosities (0.6), because input varicosity PDs were not perfectly aligned (Figure S4).

Recent experimental work and theoretical work suggest that the structure and source of noise influence the amount of information that can propagate through a neural network (Brinkman et al., 2016; Cafaro and Rieke, 2010; Moreno-Bote et al., 2014; Zylberberg et al., 2016). Here, to assess the fidelity of DS information conveyed to the DSGC by SAC varicosities, we examined two potential noise structures that could degrade the information content in SAC signals. The first, "amplitude modulation (AM)" noise, was simulated by adding normally distributed trial-to-trial variability to response amplitudes to decrease the SNR evenly across the DS tuning curve (Figure 5A<sub>1</sub>). Biological AM noise could arise due to the stochastic behavior of ion channels and synapses in the DS circuitry. A second noise structure, "direction modulation (DM)" noise, was simulated by varying the orientation of the DS tuning curve on a trial-by-trial basis (Figure 5A<sub>2</sub>). DM noise increases the  $\sigma_{PD}$  of simulated varicosities directly and could arise from instability or short-term plasticity of DS tuning (Rivlin-Etzion et al., 2012). The maximal variability potentially introduced by these noise sources could be estimated directly from our recordings: if only one or the other noise source were present, AM noise would be reflected in the SNR of varicosity responses and DM noise from the intra-varicosity  $\sigma_{PD}$  (Figures 4A and 4F).

DM-like noise has been shown to corrupt signal decoding in a network of neurons, whereas AM-like noise exerts more subtle effects (Brinkman et al., 2016; Moreno-Bote et al., 2014; Zylberberg et al., 2016). We examined the impact of both types of noise on DS signaling to test whether these insights hold true for inhibitory synaptic integration in DSGCs. We simulated individual varicosity responses in the presence of noise and then summed the SAC inputs to acquire the IPSC in the DSGC. AM noise introduced trial-to-trial variability in IPSC amplitudes (Figure 5B<sub>1</sub>), as expected, but it did not significantly reduce the average post-synaptic DS tuning (Figure 5C<sub>1</sub>). In these simulations, AM noise was imposed upon each varicosity independently; similar results were observed when noise was correlated among clusters of adjacent varicosities on individual SACs (data not shown).

By contrast, DM noise reduced mean PD IPSCs and increased mean ND IPSCs, thereby decreasing the DSI of the IPSC (Figures 5B<sub>2</sub> and 5C<sub>2</sub>). Because DM noise broadened the tuning curve and made it shallower, its impact was not alleviated by postsynaptic signal averaging: varying the number of SAC inputs had little effect on the IPSC DSI in the presence of DM noise (Figure 5C<sub>2</sub>, right). These findings echo, at the single-cell level, previous theoretical examinations of the impact of AM-like and DM-like noise on population coding (Moreno-Bote et al., 2014; Zylberberg et al., 2016).



## SAC Signals Reflect AM Noise

Our simulations highlighted two potential noise sources that are predicted to exert different effects on DS signal fidelity. We next compared the model with experimental data to identify which noise type predominates in SAC varicosities (Figure 6). Both AM and DM noise increased simulated response variability and  $\sigma_{PD}$  (Figure 6A). The SNR calculated from AM noise simulations was directly proportional to the SNR used to set the amplitude noise level, whereas  $\sigma_{PD}$  calculated in DM noise simulations was a more complicated function of the imposed  $\sigma_{PD}$  (Figure S5). Only AM noise simulations accurately reproduced our experimental results: physiological AM noise levels (SNR = 2) generated the experimentally observed  $\sigma_{PD}$  (Figure 6B<sub>1</sub>), whereas no DM noise level gave rise to the measured SNR (Figure 6B<sub>2</sub>). These results suggest that trial-to-trial variability of SAC signals is likely due to AM noise, which appears well tolerated by the postsynaptic DSGC.

Taken together, these modeling results help clarify the impact of SAC-SAC inhibition on DS signaling. Experiments with SR95531 indicated that inhibition decreases SNR but enhances DSI (i.e., the ratio of PD responses to ND responses) in individual SAC varicosities (Figures 3 and 5). Our simulations suggested that postsynaptic integration in DSGCs mitigates the impact of low SNR but not poor DSI (Figure 5). Consequently, lateral inhibition may enhance DS fidelity in DSGCs, despite no apparent improvement at the level of individual SAC varicosities.

## DISCUSSION

Our results indicate that SAC dendritic arbors comprise ~20 functionally distinct compartments, each containing 10-15 varicosities that exhibit highly correlated responses and similar DS tuning. Inhibition enhances compartmentalization and improves DS signaling primarily by keeping SAC varicosity signals near the middle of their dynamic range, thereby maximizing response correlations and the difference between PD and ND responses (Figures 2 and 3). This benefit comes at a cost—decreased SNR—that is mitigated by signal integration in the postsynaptic DSGC (Figure 5). Our results complement those from a recent study showing that another inhibitory mechanism, mediated by metabotropic glutamate receptors, prevents crosstalk between opposite sides of the SAC dendritic arbor (Koren et al., 2017). Others have shown that inhibition locally limits active dendritic conductances (Lovett-Barron et al., 2012) and controls postsynaptic responses with single-synapse specificity (Chiu et al., 2013) in hippocampal and cortical pyramidal cells, respectively. Together, these studies and our results indicate that inhibition regulates dendritic compartmentalization over a wide range of spatial scales.

### Downstream Mechanisms Sharpen DS Tuning that Originates in SAC Dendrites

DS signals originate in SAC dendritic varicosities as a result of synaptic and biophysical processes, along the length of a branching dendrite, that produce larger  $Ca^{2+}$  signals in response to centrifugal motion (Euler et al., 2002; Hausselt et al., 2007; Tukker et al., 2004; Vlasits et al., 2016). The apparent strength of this asymmetry may vary with the tool used to measure it: the genetically encoded  $Ca^{2+}$  indicator GCaMP6m produced higher DSI values in SAC dendrites than those measured with OGB1 (cf. Chen et al., 2016; Euler et al., 2002;

see also Figure 3). In either case, however, the DS tuning of individual SAC varicosities compares favorably with that of composite IPSCs recorded in DSGCs (Fried et al., 2002; Poleg-Polsky and Diamond, 2016a)—particularly considering that a nonlinear relationship between presynaptic  $\text{Ca}^{2+}$  and neurotransmitter release (Dodge and Rahamimoff, 1967) likely sharpens the DS tuning of GABA release relative to the presynaptic  $\text{Ca}^{2+}$  signals. DS fidelity is enhanced further by action potential thresholds in DSGCs (Poleg-Polsky and Diamond, 2016a), so that DSGCs typically do not spike in response to ND stimuli and exhibit tuning curves (Briggman et al., 2011; Taylor and Vaney, 2002) that are sufficiently broad to enable higher visual centers to discriminate small differences in motion direction (e.g., Butts and Goldman, 2006). Postsynaptic integration, multiple downstream nonlinearities, and the coding benefits of broad tuning curves may, therefore, relax the demand for extremely precise DS signaling in individual SAC varicosities.

### SACs Exhibit Stereotyped Dendritic Geometry

SACs exhibit distinctive dendritic morphology (e.g., Briggman et al., 2011; Euler et al., 2002; Famiglietti, 1983; Vaney, 1984), but compartmental simulations suggest that optimal DS signaling in SAC dendrites may not require particular branching patterns (Tukker et al., 2004). Our morphological analysis revealed remarkably consistent dendritic geometry across SACs (Figure S1). For example, SACs analyzed here contained  $144 \pm 10$  branch segments, a coefficient of variation (CV) ( $\text{CV} = \sigma/\text{mean} = 7\%$ ;  $n = 9$ ) that is much lower than in rat retinal AII amacrine cells (37%; Zandt et al., 2017), cat cortical stellate cells (42%; Sholl, 1953), or cat cortical pyramidal cells (30%; Sholl, 1953). The number of terminal dendritic branches also varied less in SACs (5%) than in AII cells (37%; Zandt et al., 2017). (We sampled SACs only from the central retina to minimize variability due to retinal eccentricity.) Our analysis indicates abrupt changes in response correlations at branch points (Figure 2C), but further experiments are required to identify more specific roles for dendritic architecture in SAC function.

### Lateral Inhibition Influences SAC Signaling

SACs contact each other extensively via GABAergic synapses containing  $\text{GABA}_A$  receptors (Ding et al., 2016; Kostadinov and Sanes, 2015; Lee and Zhou, 2006). SACs also contact other amacrine cells, including wide-field amacrine cells (WACs), but about 90% of their inhibitory inputs come from other SACs (Ding et al., 2016). A recent study reported little effect on DS tuning in SACs in which the *Slc32a1* vesicular GABA transporter gene or the *Gabra2* GABA receptor subunit gene had been deleted only in SACs (Chen et al., 2016). These authors observed SR95531 effects in both knockouts and suggested that WACs, rather than SACs, may provide the lateral inhibition that enhances DS. Although WACs supply only 5% of the inhibitory inputs to ON SACs, they make their inputs very close to the soma (Ding et al., 2016) and may, therefore, influence signaling throughout large regions of the SAC dendritic arbor. Our conclusions regarding inhibition's impact on SAC signaling hold, regardless of its source.

We found that inhibition enhances dendritic compartmentalization but does not define it (Figure 2). Most inhibitory inputs arrive more proximally than the demarcation of functional compartments and are not located consistently near branch points (Ding et al., 2016),

suggesting that lateral inhibition may function more as a regional gain control mechanism rather than a local gate to isolate adjacent dendritic branches from one another.

### **DSGC Integration Mitigates Noisy Signals in SAC Varicosities**

Our findings are consistent with previous theoretical analyses of noise processing in neural circuitry (Brinkman et al., 2016; Moreno-Bote et al., 2014; Zylberberg et al., 2016), and they indicate that those authors' insights regarding the information carried by noisy signals in a neural population apply to the integration of noisy synaptic inputs within a single cell. Our simulations also provide an intuitive explanation for how one particular type of corruptive noise would reduce the information that can be decoded by the receiver. DM noise, which shifts the peak of the DS tuning curve of individual SAC varicosities, was chosen because PD in SAC dendrites can switch following visual adaptation (Rivlin-Etzion et al., 2012) and, therefore, may possibly vary on a shorter term basis. We did not detect evidence for DM noise in our recordings, however, suggesting that DS tuning remains consistent in the absence of adaptive changes.

DM is but one of multiple noise types that can negatively affect neural information processing. In general, harmful noise sources lead to activity patterns that mimic noise-free responses, because the consequent uncertainty about the nature of the stimulus diminishes the amount of information that can be extracted from the signal. Recent analyses of the relationship between stimulus-dependent correlations and efficient coding argued that noise lying along the information plane—namely, the set of all possible responses under noise-free conditions—interferes with signaling to a much greater extent than noise oriented perpendicularly to the information plane (Brinkman et al., 2016; Moreno-Bote et al., 2014; Zylberberg et al., 2016). For example, correlated noise within a SAC functional compartment could disrupt downstream signaling if many of the correlated synapses contacted the same postsynaptic DSGC. Dense anatomical reconstruction of SAC-DSGC connectivity indicated, however, that neighboring SAC varicosities typically target different postsynaptic cells and that each DSGC receives input from 10-20 different SACs (Briggman et al., 2011). We suspect, therefore, that correlated noise in adjacent SAC varicosities has, at most, only a minor impact on signal fidelity in DSGCs. Accordingly, our model did not require correlations between SAC varicosities to replicate experimental results and highlighted the power of synaptic integration to extract relevant signal from noisy individual synaptic inputs.

### **Potential Signaling Benefits of SAC Compartmentalization**

Noise is generally thought to degrade information transfer through a network, but correlated variability may, in some cases, actually increase coding accuracy (Abbott and Dayan, 1999). In single DSGCs, correlations between excitatory and inhibitory inputs, presumably due to common presynaptic circuitry, enhance the fidelity of DS tuning because correlated (non-DS) noise cancels each other out, enabling more sensitive detection of directional information (Cafaro and Rieke, 2010; Zylberberg et al., 2016). Excitatory-inhibitory correlations presumably would be maximized if each were driven by common populations of presynaptic bipolar cells (Cafaro and Rieke, 2010). If functional compartments within each SAC encompassed entire quadrants of the dendritic arbor, however, the RF of each

inhibitory input from a SAC synaptic varicosity would be substantially larger than those of excitatory inputs from individual bipolar cells (FWHM, ~100  $\mu\text{m}$ ; Franke et al., 2017). Instead, compartmentalization diminishes the spatial extent of SAC varicosity RFs to dimensions that are more comparable to those of excitatory RFs. Even though SAC inputs and outputs are spatially offset (Ding et al., 2016), and SAC varicosity RFs are more elliptical than those of bipolar cells, the similar RF dimensions may enhance excitatory-inhibitory (E-I) correlations, particularly in response to ND stimuli (Cafaro and Rieke, 2010).

## EXPERIMENTAL PROCEDURES

### Tissue Dissection, Calcium Indicator Loading, and Imaging

Animal procedures were conducted according to NIH guidelines and approved by the NINDS Animal Care and Use Committee (ASP 1361). ChAT-tdTomato mice (postnatal day [P]30–P60, both sexes, Jackson Laboratory) were anesthetized with isoflurane (Baxter) inhalation and killed by decapitation. Retinas were isolated, and subsequent procedures were performed at room temperature in Ames media (Sigma) equilibrated with 95%  $\text{O}_2$ /5%  $\text{CO}_2$ . tdTomato<sup>+</sup> SACs in central retina were visualized in whole-mount central retina (<1 mm from optic disk) via fluorescence and were impaled with sharp electrodes (100–150  $\text{M}\Omega$ ) containing OGB1 (Life Technologies, 15 mM in water). OGB1 was delivered via iontophoretic voltage pulses (50 ms, 15 V peak-to-peak (p-p), 10-kHz square wave). The electrode was withdrawn as soon as the cell body began to fill with fluorescent dye; recording commenced following a ~30-min interval to allow the dye to fill the dendrites.

Two-photon imaging was performed using a microscope (Sutter Instruments) controlled by ScanImage (Vidrio Technologies) and equipped with a 20 $\times$ /0.95 NA objective (Olympus) and photomultiplier tubes filtered to detect green (500–540 nm) and red (575–640 nm) fluorescence excited by 920-nm laser light (Chameleon Ti:S, Coherent). OGB1  $\text{Ca}^{2+}$  signals were obtained at a 10-Hz frame rate (pixel x-y resolution: 0.3125  $\times$  0.625  $\mu\text{m}$ ). To reconstruct SAC morphology, z stacks (50–75 z slices, 3–5 images averaged at each z level) were collected at 1- $\mu\text{m}$  z intervals.

### Light Stimulation

Light stimuli were generated with custom software (Igor Pro, Wavemetrics; Workshop 4 IDE, 4D Systems) to control an LCD screen masking a collimated LED (405 nm, Thorlabs). Stimuli were projected through the objective. For motion stimuli, a 400- $\mu\text{m}$   $\times$  400- $\mu\text{m}$  bar ( $\sim 25 \times 10^3$  photons  $\text{s}^{-1} \mu\text{m}^{-2}$  on a background of  $\sim 6 \times 10^3$  photons  $\text{s}^{-1} \mu\text{m}^{-2}$ ) was translated across the entire field in each of eight evenly spaced directions (3–6 rounds of stimuli in each experimental condition) at 1 mm  $\text{s}^{-1}$ . Stationary bar stimuli used for receptive field mapping were 20  $\times$  400  $\mu\text{m}$  (same intensity and contrast), presented at 13 different positions evenly spaced at 25- $\mu\text{m}$  intervals across the visual field and rotated by 5 evenly spaced (45 $^\circ$ ) angles.

### Calcium-Imaging Data Analysis

The x-y-t image stacks were analyzed using custom software (Igor Pro). Images were segmented via simple thresholding, and regions of interest (ROIs) circumscribed individual

varicosities. Responses were quantified as the average  $F/F$  during 1 s after stimulus onset relative to a pre-stimulus baseline. Two-dimensional RFs of individual varicosities were determined as described previously (Johnston et al., 2014) and fit with a two-dimensional Gaussian function; the FWHM of the RF was calculated as:

$$FWHM = \sqrt{2 \ln 2} (\sigma_x + \sigma_y),$$

where  $\sigma_x$  and  $\sigma_y$  are the Gaussian space constants generated by the fit. The DSI was calculated as  $DSI = (R_{PD} - R_{ND})/R_{PD}$ , where  $R_{PD}$  and  $R_{ND}$  are the responses to PD and ND stimuli, respectively. This calculation was favored over an alternative ( $(R_{PD} - R_{ND})/(R_{PD} + R_{ND})$ ), because it was more robust to negative  $R_{ND}$  values occasionally encountered in noisy OGB1 signals.

Agglomerative hierarchical clustering (Figure 2) was performed in MATLAB (using clusterdata and the Calinski-Harabz criterion) on an  $m \times n$  matrix representing single-trial responses in each varicosity ( $m$  varicosities,  $n$  trials). The illustrated pairwise correlation coefficient ( $r_{i,j}$ ) between each pair of varicosities was calculated by:

$$r_{i,j} = \frac{\sum (R_i - \bar{R}_i)(R_j - \bar{R}_j)}{\sqrt{\sum (R_i - \bar{R}_i)^2} \sqrt{\sum (R_j - \bar{R}_j)^2}},$$

where  $R_i$  and  $R_j$  are individual responses of varicosities  $i$  and  $j$  and  $\bar{R}_i$  and  $\bar{R}_j$  are average responses.

### Modeling of SAC Varicosity Responses and Synaptic Integration in DSGC

100 SACs were distributed with a spacing of  $50 \pm 20 \mu\text{m}$  (mean  $\pm$  SD) over an area of  $500 \times 500 \mu\text{m}$ . Each SAC contained 180 varicosities, arranged evenly on the circumference of a  $120\text{-}\mu\text{m}$ -radius circle around the SAC center. SAC varicosities contacted the DSGC stochastically, according to a normal probability distribution of their anatomical angle, scaled to obtain a realistic number of presynaptic inputs (Figure S4B; Briggman et al., 2011). The stimulus was simply a direction of activation. Varicosity tuning profiles were modeled as a Gaussian centered about their anatomical orientation relative to the soma ( $DSI = 0.66$ ,  $FWHM = 100^\circ$ ). Noise sources were simulated independently for each varicosity and for each trial.

Unless indicated otherwise, data are expressed as mean  $\pm$  SD, and statistically significant differences (t test) were concluded if  $p < 0.05$ .

### Supplementary Material

Refer to Web version on PubMed Central for supplementary material.

## Acknowledgments

We thank Ms. Hua Tian for mouse husbandry; Dr. Espen Hartveit for personal communication regarding AII amacrine cell morphology; and Drs. Cole Graydon, William Grimes, Fred Rieke, Miloslav Sedlacek, and Joel Zylberberg for comments on the manuscript. This work was supported by the NINDS Intramural Research Program (NS003145).

## References

- Abbott LF, Dayan P. The effect of correlated variability on the accuracy of a population code. *Neural Comput.* 1999; 11:91–101. [PubMed: 9950724]
- Behrens C, Schubert T, Haverkamp S, Euler T, Berens P. Connectivity map of bipolar cells and photoreceptors in the mouse retina. *eLife.* 2016; 5:e20041. [PubMed: 27885985]
- Branco T, Clark BA, Häusser M. Dendritic discrimination of temporal input sequences in cortical neurons. *Science.* 2010; 329:1671–1675. [PubMed: 20705816]
- Briggman KL, Helmstaedter M, Denk W. Wiring specificity in the direction-selectivity circuit of the retina. *Nature.* 2011; 471:183–188. [PubMed: 21390125]
- Brinkman BA, Weber AI, Rieke F, Shea-Brown E. How do efficient coding strategies depend on origins of noise in neural circuits? *PLoS Comput Biol.* 2016; 12:e1005150. [PubMed: 27741248]
- Butts DA, Goldman MS. Tuning curves, neuronal variability, and sensory coding. *PLoS Biol.* 2006; 4:e92. [PubMed: 16529529]
- Cafaro J, Rieke F. Noise correlations improve response fidelity and stimulus encoding. *Nature.* 2010; 468:964–967. [PubMed: 21131948]
- Chen Q, Pei Z, Koren D, Wei W. Stimulus-dependent recruitment of lateral inhibition underlies retinal direction selectivity. *eLife.* 2016; 5:e21053. [PubMed: 27929372]
- Chiu CQ, Lur G, Morse TM, Carnevale NT, Ellis-Davies GC, Higley MJ. Compartmentalization of GABAergic inhibition by dendritic spines. *Science.* 2013; 340:759–762. [PubMed: 23661763]
- Ding H, Smith RG, Poleg-Polsky A, Diamond JS, Briggman KL. Species-specific wiring for direction selectivity in the mammalian retina. *Nature.* 2016; 535:105–110. [PubMed: 27350241]
- Dodge FA Jr, Rahamimoff R. Co-operative action a calcium ions in transmitter release at the neuromuscular junction. *J Physiol.* 1967; 193:419–432. [PubMed: 6065887]
- Eggers ED, Lukasiewicz PD. Multiple pathways of inhibition shape bipolar cell responses in the retina. *Vis Neurosci.* 2011; 28:95–108. [PubMed: 20932357]
- Euler T, Detwiler PB, Denk W. Directionally selective calcium signals in dendrites of starburst amacrine cells. *Nature.* 2002; 418:845–852. [PubMed: 12192402]
- Famiglietti EV Jr. ‘Starburst’ amacrine cells and cholinergic neurons: mirror-symmetric on and off amacrine cells of rabbit retina. *Brain Res.* 1983; 261:138–144. [PubMed: 6301622]
- Famiglietti EV. Synaptic organization of starburst amacrine cells in rabbit retina: analysis of serial thin sections by electron microscopy and graphic reconstruction. *J Comp Neurol.* 1991; 309:40–70. [PubMed: 1894768]
- Franke K, Berens P, Schubert T, Bethge M, Euler T, Baden T. Inhibition decorrelates visual feature representations in the inner retina. *Nature.* 2017; 542:439–444. [PubMed: 28178238]
- Fransen JW, Borghuis BG. Temporally diverse excitation generates direction-selective responses in ON- and OFF-type retinal starburst amacrine cells. *Cell Rep.* 2017; 18:1356–1365. [PubMed: 28178515]
- Fried SI, Münch TA, Werblin FS. Mechanisms and circuitry underlying directional selectivity in the retina. *Nature.* 2002; 420:411–414. [PubMed: 12459782]
- Gavrikov KE, Dmitriev AV, Keyser KT, Mangel SC. Cationchloride cotransporters mediate neural computation in the retina. *Proc Natl Acad Sci USA.* 2003; 100:16047–16052. [PubMed: 14665697]
- Grimes WN, Zhang J, Graydon CW, Kachar B, Diamond JS. Retinal parallel processors: more than 100 independent microcircuits operate within a single interneuron. *Neuron.* 2010; 65:873–885. [PubMed: 20346762]



- Hartline HK. The response of single optic nerve fibers of the vertebrate eye to illumination of the retina. *Am J Physiol.* 1938; 121:400–415.
- Hausselt SE, Euler T, Detwiler PB, Denk W. Adendrite-autonomous mechanism for direction selectivity in retinal starburst amacrine cells. *PLoS Biol.* 2007; 5:e185. [PubMed: 17622194]
- Häusser M, Mel B. Dendrites: bug or feature? *Curr Opin Neurobiol.* 2003; 13:372–383. [PubMed: 12850223]
- Ivanova E, Hwang GS, Pan ZH. Characterization of transgenic mouse lines expressing Cre recombinase in the retina. *Neuroscience.* 2010; 165:233–243. [PubMed: 19837136]
- Johnston J, Ding H, Seibel SH, Esposti F, Lagnado L. Rapid mapping of visual receptive fields by filtered back projection: application to multi-neuronal electrophysiology and imaging. *J Physiol.* 2014; 592:4839–4854. [PubMed: 25172952]
- Kim JS, Greene MJ, Zlateski A, Lee K, Richardson M, Turaga SC, Purcaro M, Balkam M, Robinson A, Behabadi BF, et al. EyeWriters. Space-time wiring specificity supports direction selectivity in the retina. *Nature.* 2014; 509:331–336. [PubMed: 24805243]
- Koren D, Grove JCR, Wei W. Cross-compartmental modulation of dendritic signals for retinal direction selectivity. *Neuron.* 2017; 95:914–927.e4. [PubMed: 28781167]
- Kostadinov D, Sanes JR. Protocadherin-dependent dendritic self-avoidance regulates neural connectivity and circuit function. *eLife.* 2015; 4:e08964.
- Kuffler SW. Discharge patterns and functional organization of mammalian retina. *J Neurophysiol.* 1953; 16:37–68. [PubMed: 13035466]
- Lee S, Zhou ZJ. The synaptic mechanism of direction selectivity in distal processes of starburst amacrine cells. *Neuron.* 2006; 51:787–799. [PubMed: 16982423]
- Lee S, Kim K, Zhou ZJ. Role of ACh-GABA cotransmission in detecting image motion and motion direction. *Neuron.* 2010; 68:1159–1172. [PubMed: 21172616]
- London M, Häusser M. Dendritic computation. *Annu Rev Neurosci.* 2005; 28:503–532. [PubMed: 16033324]
- Lovett-Barron M, Turi GF, Kaifosh P, Lee PH, Bolze F, Sun XH, Nicoud JF, Zemelman BV, Sternson SM, Losonczy A. Regulation of neuronal input transformations by tunable dendritic inhibition. *Nat Neurosci.* 2012; 15:423–430. [PubMed: 22246433]
- Masland RH. The many roles of starburst amacrine cells. *Trends Neurosci.* 2005; 28:395–396. [PubMed: 15979167]
- McClain JO, Rao VR. CLUSTISZ: a program to test for the quality of clustering of a set of objects. *J Mark Res.* 1975; 12:456–460.
- Moreno-Bote R, Beck J, Kanitscheider I, Pitkow X, Latham P, Pouget A. Information-limiting correlations. *Nat Neurosci.* 2014; 17:1410–1417. [PubMed: 25195105]
- Münch TA, Werblin FS. Symmetric interactions within a homogeneous starburst cell network can lead to robust asymmetries in dendrites of starburst amacrine cells. *J Neurophysiol.* 2006; 96:471–477. [PubMed: 16598066]
- Oesch NW, Taylor WR. Tetrodotoxin-resistant sodium channels contribute to directional responses in starburst amacrine cells. *PLoS ONE.* 2010; 5:e12447. [PubMed: 20805982]
- Poleg-Polsky A, Diamond JS. NMDA receptors multiplicatively scale visual signals and enhance directional motion discrimination in retinal ganglion cells. *Neuron.* 2016a; 89:1277–1290. [PubMed: 26948896]
- Poleg-Polsky A, Diamond JS. Retinal circuitry balances contrast tuning of excitation and inhibition to enable reliable computation of direction selectivity. *J Neurosci.* 2016b; 36:5861–5876. [PubMed: 27225774]
- Rivlin-Etzion M, Wei W, Feller MB. Visual stimulation reverses the directional preference of direction-selective retinal ganglion cells. *Neuron.* 2012; 76:518–525. [PubMed: 23141064]
- Sholl DA. Dendritic organization in the neurons of the visual and motor cortices of the cat. *J Anat.* 1953; 87:387–406. [PubMed: 13117757]
- Stuart GJ, Spruston N. Dendritic integration: 60 years of progress. *Nat Neurosci.* 2015; 18:1713–1721. [PubMed: 26605882]

- Taylor WR, Vaney DI. Diverse synaptic mechanisms generate direction selectivity in the rabbit retina. *J Neurosci.* 2002; 22:7712–7720. [PubMed: 12196594]
- Tukker JJ, Taylor WR, Smith RG. Direction selectivity in a model of the starburst amacrine cell. *Vis Neurosci.* 2004; 21:611–625. [PubMed: 15579224]
- Vaney DI. ‘Coronate’ amacrine cells in the rabbit retina have the ‘starburst’ dendritic morphology. *Proc R Soc Lond B Biol Sci.* 1984; 220:501–508. [PubMed: 6142459]
- Vaney DI, Sivyer B, Taylor WR. Direction selectivity in the retina: symmetry and asymmetry in structure and function. *Nat Rev Neurosci.* 2012; 13:194–208. [PubMed: 22314444]
- Vlasits AL, Morrie RD, Tran-Van-Minh A, Bleckert A, Gainer CF, DiGregorio DA, Feller MB. A role for synaptic input distribution in a dendritic computation of motion direction in the retina. *Neuron.* 2016; 89:1317–1330. [PubMed: 26985724]
- Werblin FS, Dowling JE. Organization of the retina of the mud-puppy, *Necturus maculosus*. II. Intracellular recording. *J Neurophysiol.* 1969; 32:339–355. [PubMed: 4306897]
- Zandt BJ, Liu JH, Veruki ML, Hartveit E. AII amacrine cells: quantitative reconstruction and morphometric analysis of electrophysiologically identified cells in live rat retinal slices imaged with multi-photon excitation microscopy. *Brain Struct Funct.* 2017; 222:151–182. [PubMed: 26951289]
- Zylberberg J, Cafaro J, Turner MH, Shea-Brown E, Rieke F. Direction-selective circuits shape noise to ensure a precise population code. *Neuron.* 2016; 89:369–383. [PubMed: 26796691]

**Highlights**

- Visual responses of many individual synapses were measured simultaneously
- SAC dendrites contain many functionally distinct clusters of output synapses
- Inhibition enhances dendritic compartmentalization and directional tuning
- SAC signaling noise is well tolerated via postsynaptic integration in DSGCs

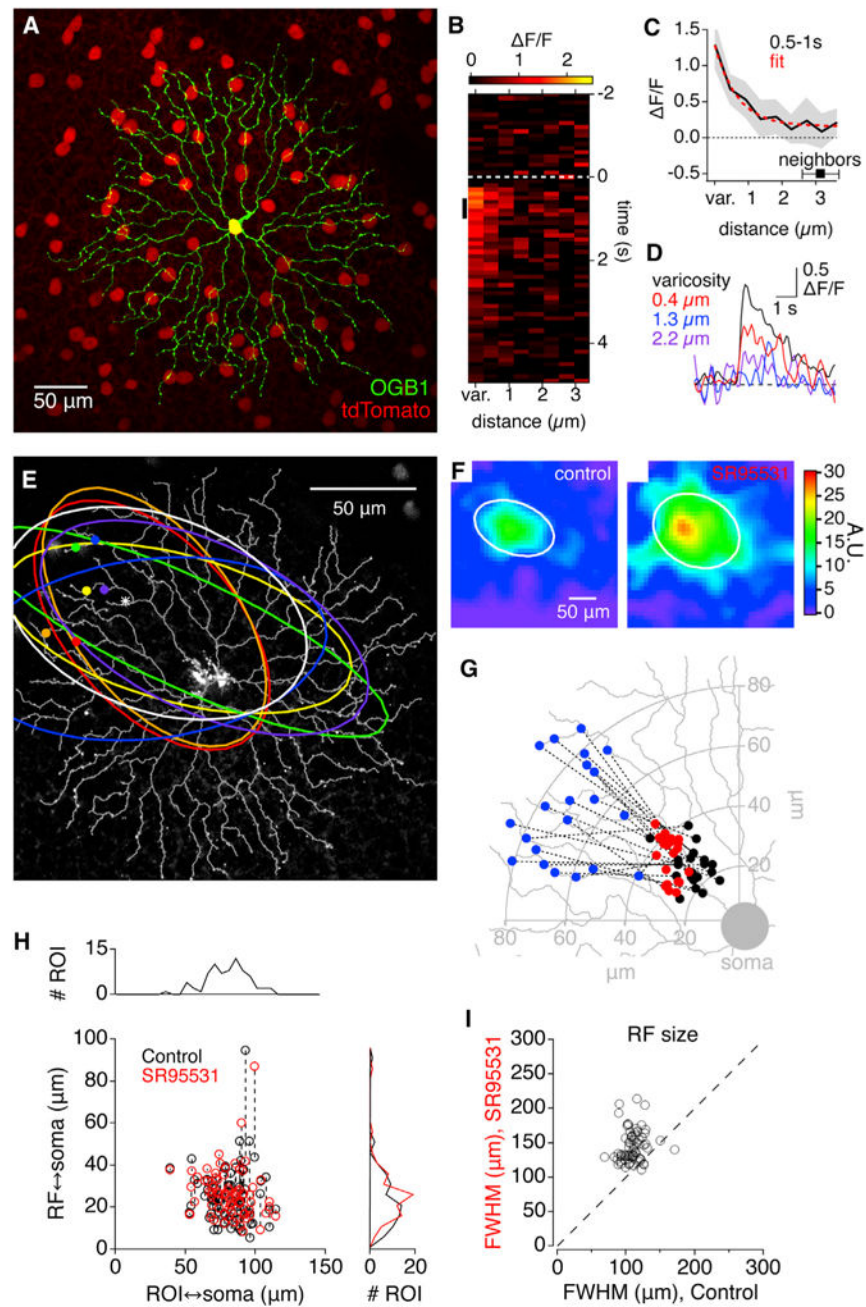


**Figure 1. Visual RFs of Individual SAC Varicosities**

(A) Fluorescence micrograph of a flat-mount mouse retina expressing tdTomato (red) in SACs under control of the ChAT promoter. One SAC (green) has been filled with OGB1. (B)  $x-t$  plot showing the spatiotemporal profile of visually evoked OGB1  $\text{Ca}^{2+}$  signals averaged from 10 different varicosities on the same SAC. (C) Average decay of OGB1 fluorescence with distance from the 10 varicosities in (B) over the time interval indicated by the black vertical line in (B). Red line indicates exponential fit. Average distance between varicosities is indicated for comparison. Distances were measured from the center of the varicosity. (D) Average decay of OGB1 fluorescence with distance for three varicosities (0.4  $\mu\text{m}$ , 1.3  $\mu\text{m}$ , 2.2  $\mu\text{m}$ ). (E) Fluorescence micrograph of a flat-mount mouse retina showing multiple varicosities (colored) and their visual RFs (colored ellipses). (F) Heatmaps of visual RFs for control (left) and SR95531 (right) conditions. (G) Schematic diagram of visual RFs for control (blue) and SR95531 (red) conditions. (H) Scatter plot of RF size vs. distance from soma for control (black) and SR95531 (red) conditions. (I) Scatter plot of FWHM for SR95531 vs. FWHM for control conditions.

- (D) Average  $F/F$  for the 10 varicosities versus time at 3 different distances from the varicosity center.
- (E) Fluorescence micrograph of OGB1-filled SAC, with traced dendrites superimposed (gray). Symbols indicate representative individual varicosities, and the correspondingly colored ellipses indicate the half-maximal isobar of the measured RF.
- (F) Example RFs, from the varicosity marked with an asterisk in (E), in control solutions (left) and in the presence of SR95531 (right). White ellipses indicate the half-maximal contour of a two-dimensional Gaussian fit.
- (G) Location of RF centers, in control conditions (black) and in the presence of SR95531 (red) relative to the physical location of the varicosity (blue).
- (H) Comparison of distances between the RF center and the varicosity (ROI), relative to the soma. Dashed lines connect control and SR95531 values from the same cell.
- (I) Comparison of RF size (FWHM) in control and in the presence of SR95531.
- See also Figures S1 and S2.

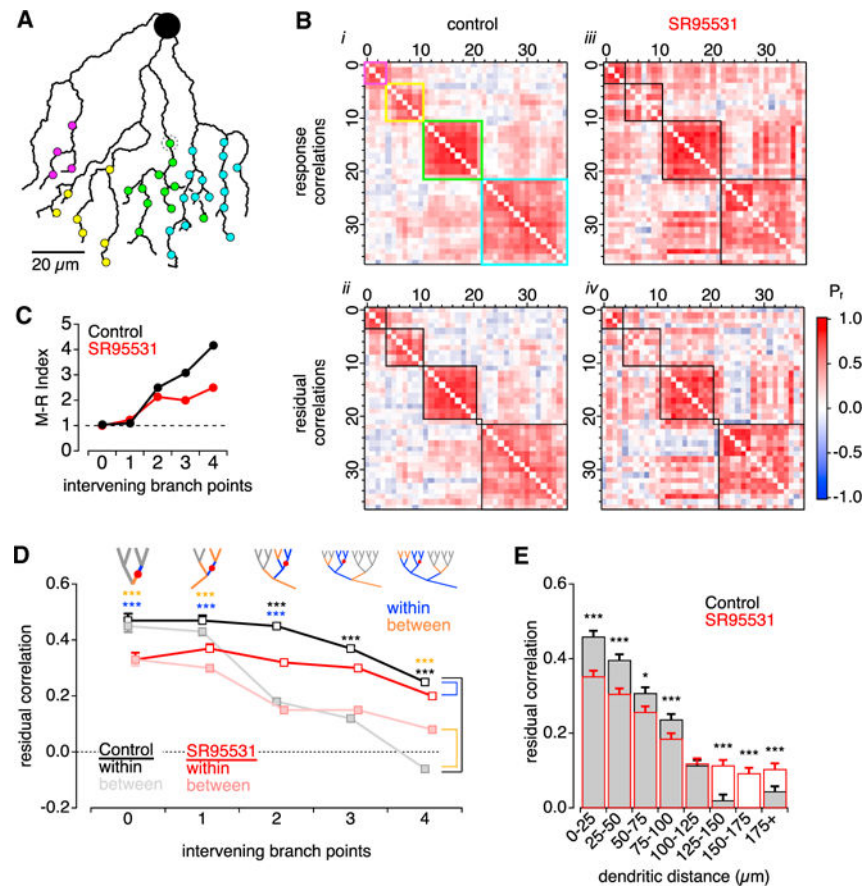


**Figure 2. Neighboring Varicosities Exhibit Correlated Responses to Visual Stimuli**

(A) Schematic tracing of a SAC dendritic region studded with synaptic varicosities (circles).

(B) Matrices showing pairwise response correlation coefficients between the 38 varicosities shown in (A). (i) Hierarchical clustering of varicosities based on response amplitudes in control conditions. Cluster box colors correspond to varicosities in (A). (ii) Clusters based on residual correlations in control conditions. Functional clustering was altered in only one (gray dotted circle in A). (iii and iv) Same as in (i) and (ii) but in the presence of SR95531.

(C) McClain-Rao (M-R) index, indicating the ratio of correlations within and between varicosities, versus the number of branch points separating the varicosities. Derived from data in (D) ( $n = 9$  SACs).

(D) Correlations within and between varicosities, versus number of intervening branch points, under control conditions and in the presence of SR95531. Top: schematics showing branches designated “within” and “between” for one example varicosity. The number of comparisons (within, between) of varicosities across 9 SACs for 0 to 4 intervening branch points were (26, 39), (110, 121), (322, 759), (783, 793), and (794, 781), respectively. Asterisks indicate  $p < 0.001$ : black indicates within (control) versus between (control); blue indicates within (control) versus within (SR95531); orange indicates between (control) versus between (SR95531).

(E) Residual correlations between pairs of varicosities versus dendritic distance between the pair ( $n = 9$  SACs). \* $p < 0.05$ .



\*\*\* $p < 0.001$  control versus SR95531,  $z$  test with Bonferroni multiple comparisons correction.

Author Manuscript

Author Manuscript

Author Manuscript

Author Manuscript

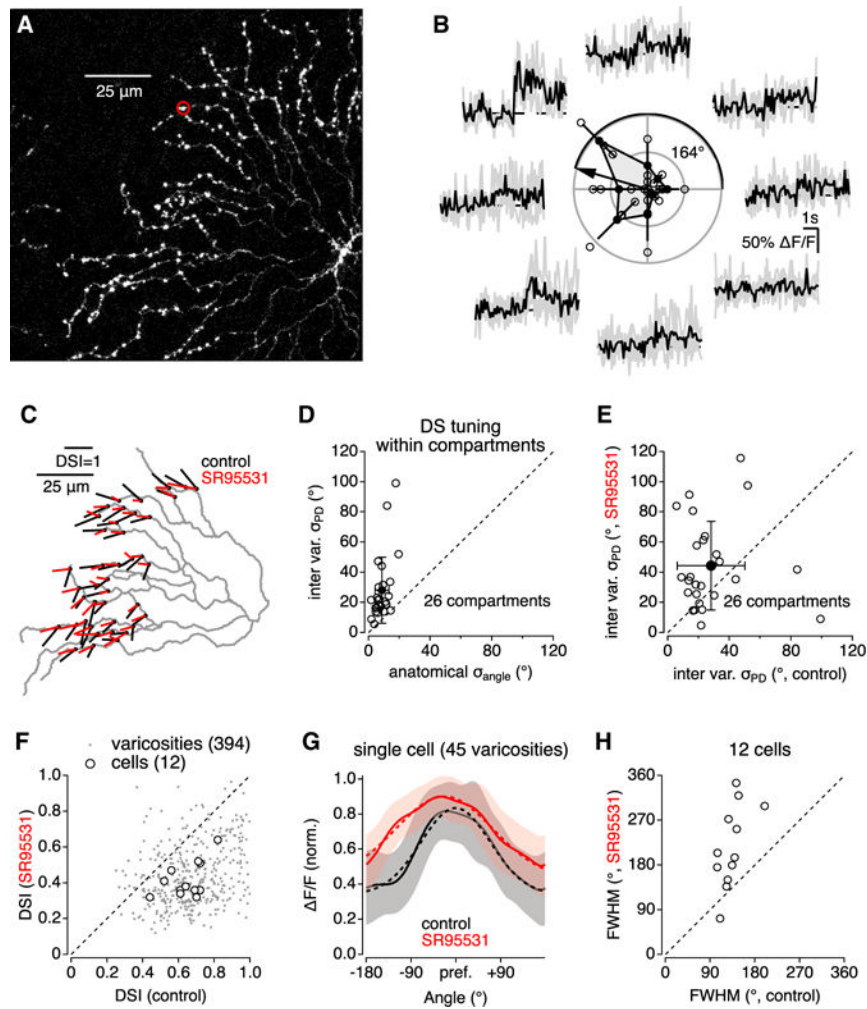


**Figure 3. Neighboring Varicosities Exhibit Variable Direction Preference**

(A) Fluorescence micrograph of OGB1-filled SAC.

(B)  $\text{Ca}^{2+}$  signals in on varicosity (circled in A) evoked by light bars moving in eight different directions. Polar plot in center indicates individual response amplitudes (open circles), mean amplitudes ( $\pm$ SD) (filled circles), and vector sum oriented toward the PD.

(C) Summarized DS tuning for each of 45 varicosities on the cell in (A). Each vector originates from a measured varicosity; the amplitude and orientation of each vector correspond to the DSI and PD, respectively.

(D) PD variability between varicosities within functional compartments was larger than the range of geometric angles relative to the soma ( $n = 26$  compartments;  $p = 3 \times 10^{-5}$ , paired t test).

(E) SR95531 increased PD variability between varicosities within individual functional compartments.

(F) Comparison of DSI in control conditions and in the presence of SR95531.

(G) Average ( $\pm$ SD, shaded) DS tuning curve of 45 varicosities recorded from the SAC in (A) in control and in the presence of SR95531.

(H) Summary scatterplot indicating effect of SR95531 on DS tuning width.

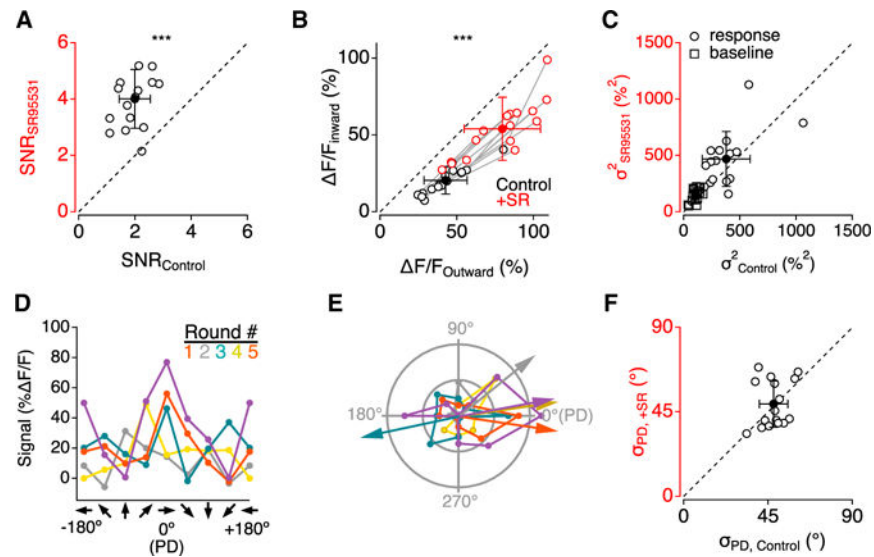


#### Figure 4. Synaptic Inhibition Decreases SNR

Throughout the figure, open symbols indicate mean values within each cell, and filled symbols indicate mean ( $\pm$ SD) across 16 SACs.

(A) Average SNR of PD responses from varicosities in 16 SACs in control and in the presence of SR95531.

(B)  $\text{Ca}^{2+}$  signals evoked by motion in both the inward (left axis) and in the outward (bottom axis) directions in control (black) and in the presence of SR95531 (red).

(C) Trial-to-trial baseline and response variance in 16 SACs were similar in control and in the presence of SR95531.

(D) Tuning curves of  $\text{Ca}^{2+}$  signals from a single varicosity for 5 rounds of stimulation with bars moving in 8 different directions.

(E) Polar plots and calculated PD for the tuning curves in (D).

(F) Variability in PD ( $\sigma_{\text{PD}}$ ), derived from repeated rounds of directional stimuli.

See also Figure S3.

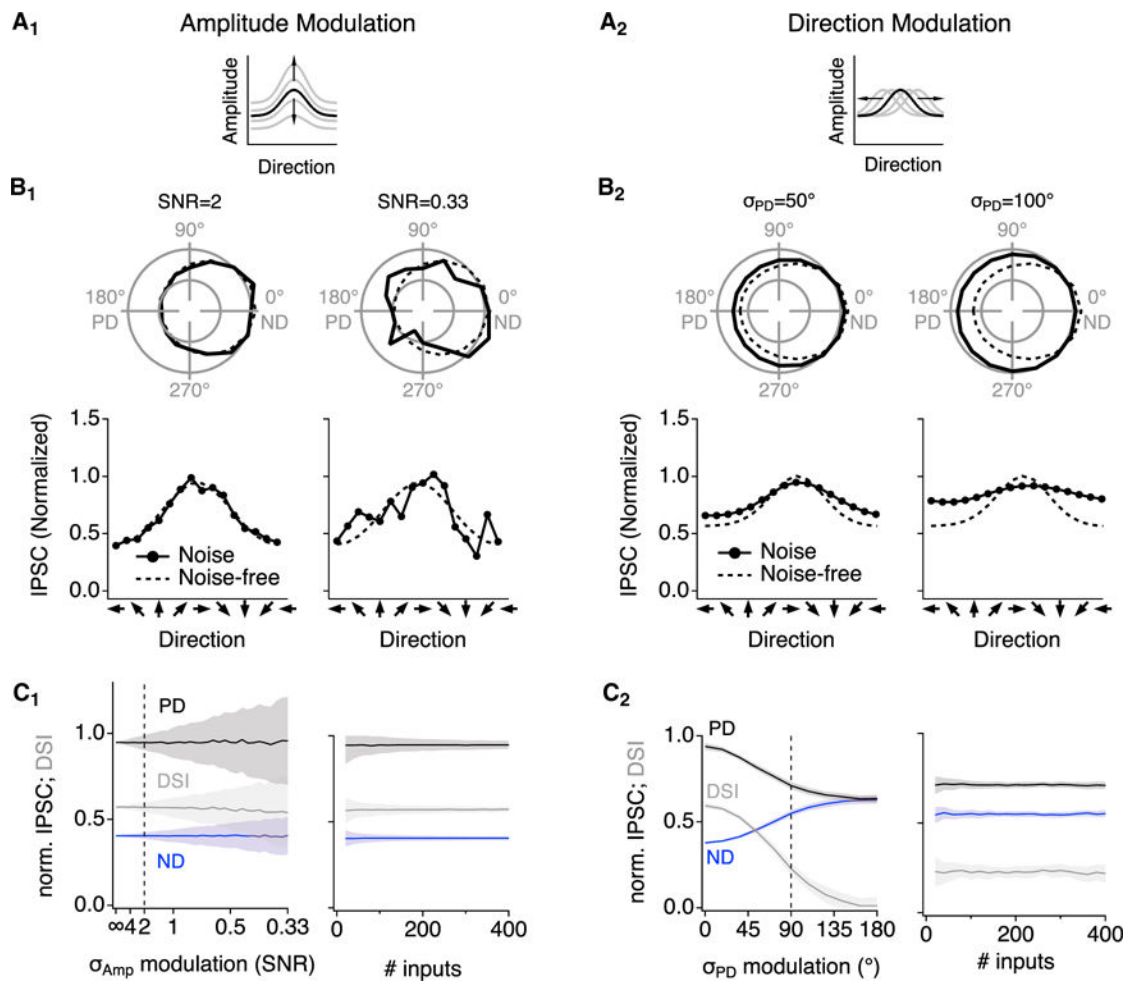


**Figure 5. Simulated Impact of Noisy SAC Signals on DSGC Signaling**

(A) Schematic illustrations of simulated AM noise (A<sub>1</sub>) and DM noise (A<sub>2</sub>).

(B) Example simulated DS tuning plots for DSGC IPSCs in the presence of AM (B<sub>1</sub>) and DM noise (B<sub>2</sub>). Parameters were set to replicate experimental SNR and  $\sigma_{PD}$ , respectively (left) (see Figure 6), and also higher noise levels (right). Dashed lines indicate approximations of the average tuning curve measured experimentally (Figure 3G).

(C) Left panels: simulated IPSC amplitudes and calculated inhibitory DSI at different levels of AM noise (C<sub>1</sub>) and DM noise (C<sub>2</sub>). DSI was robust to AM noise but not to DM noise. Right panels: simulated IPSC amplitudes and DSI at experimental noise levels (dashed lines in left panels) for varied numbers of synaptic inputs.

See also Figures S4 and S5.

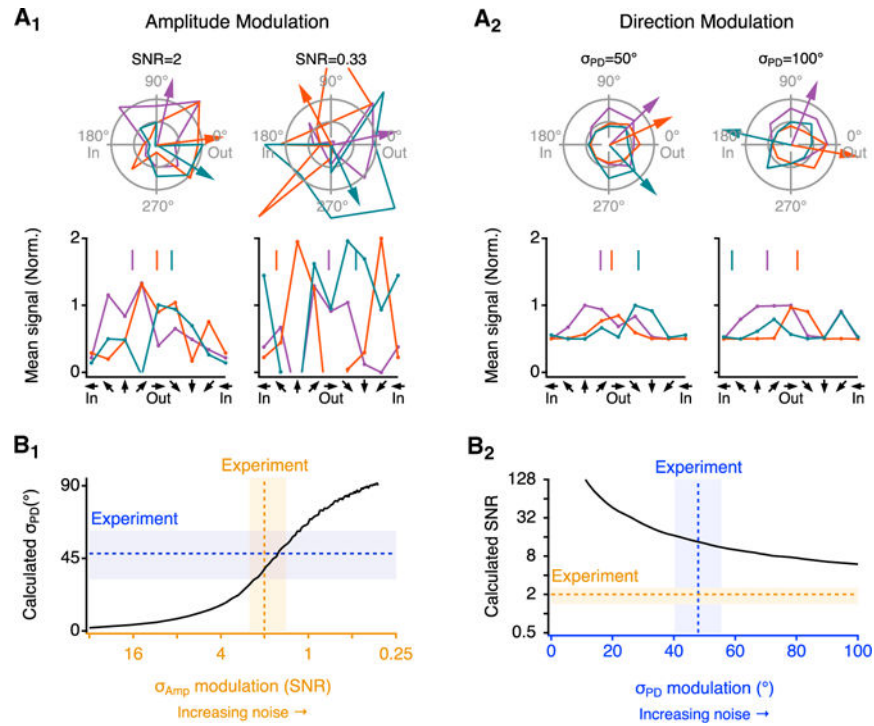


**Figure 6. SAC Signal Variability Is Attributable to AM Noise**

(A) Example effects of noise on response amplitudes from a simulated SAC varicosity. Three representative simulation rounds are indicated by separate colors. Arrows (top) and vertical lines (bottom) point to the estimated PD from each round. Noise-free PD is 0° (“Out”). Parameters for AM (A<sub>1</sub>) and DM (A<sub>2</sub>) noise types were set to replicate experimental SNR and  $\sigma_{PD}$ , respectively (left), and higher noise levels (right). (B) Response variability at different noise levels (B<sub>1</sub>, AM noise; B<sub>2</sub>, DM noise). In (B<sub>1</sub>),  $\sigma_{PD}$  was determined from 1,000 single-round repeats at each indicated SNR level. In (B<sub>2</sub>), SNR was calculated from 1,000 simulated responses to motion at PD (0°) at each  $\sigma_{PD}$  level. Dotted lines and shaded areas indicate the experimentally measured values (mean  $\pm$  SD). See also Figure S5.